The Astrophysical Journal, 698:1244–1260, 2009 June 20 doi:10.1088/0004-637X/698/2/1244

SPITZER MAPPING OF MOLECULAR HYDROGEN PURE ROTATIONAL LINES IN NGC 1333: A DETAILED STUDY OF FEEDBACK IN STAR FORMATION

Sébastien Maret[9], Edwin A. Bergin[1], David A. Neufeld[2], Joel D. Green[3], Dan M. Watson[3], Martin O. Harwit[5], Lars E. Kristensen[6], Gary J. Melnick[7], Paule Sonnentrucker[2], Volker Tolls[7], Michael W. Werner[8], Karen Willacy[8], and Yuan Yuan[2]

[1] Department of Astronomy, University of Michigan, 500 Church Street, Ann Arbor, MI 48109-1042, USA
[2] Department of Physics and Astronomy, John Hopkins University, 3400 North Charles Street, Baltimore, MD 21218, USA
[3] Department of Physics and Astronomy, University of Rochester, Rochester, NY 14627, USA
[4] Department of Astronomy, Cornell University, Ithaca, NY 14853-6801, USA
[5] 511 H Street SW, Washington, DC 20024-2725, USA
[6] Leiden Observatory, P.O. Box 9513, NL-2300 RA Leiden, Netherlands
[7] Harvard-Smithsonian Center for Astrophysics, 60 Garden Street, Cambridge, MA 02138, USA
[8] Jet Propulsion Laboratory, 4800 Oak Grove Drive, Pasadena, CA 91109, USA
Received 2009 January 7; accepted 2009 April 8; published 2009 May 28

ABSTRACT

We present mid-infrared spectral maps of the NGC 1333 star-forming region, obtained with the infrared spectrometer on board the *Spitzer Space Telescope*. Eight pure H_2 rotational lines, from $S(0)$ to $S(7)$, are detected and mapped. The H_2 emission appears to be associated with the warm gas shocked by the multiple outflows present in the region. A comparison between the observed intensities and the predictions of detailed shock models indicates that the emission arises in both slow (12–24 km s^{-1}) and fast (36–53 km s^{-1}) C-type shocks with an initial ortho-to-para ratio (*opr*) $\lesssim$1. The present H_2 *opr* exhibits a large degree of spatial variations. In the postshocked gas, it is usually about 2, i.e., close to the equilibrium value ($\sim$3). However, around at least two outflows, we observe a region with a much lower ($\sim$0.5) *opr*. This region probably corresponds to gas which has been heated up recently by the passage of a shock front, but whose ortho-to-para has not reached equilibrium yet. This, together with the low initial *opr* needed to reproduce the observed emission, provide strong evidence that H_2 is mostly in para form in cold molecular clouds. The H_2 lines are found to contribute to 25%–50% of the total outflow luminosity, and thus can be used to ascertain the importance of star formation feedback on the natal cloud. From these lines, we determine the outflow mass loss rate and, indirectly, the stellar infall rate, the outflow momentum and the kinetic energy injected into the cloud over the embedded phase. The latter is found to exceed the binding energy of individual cores, suggesting that outflows could be the main mechanism for core disruption.

Key words: astrochemistry – ISM: abundances – ISM: individual (NGC 1333) – ISM: molecules – stars: formation

Online-only material: color figures, extended figure

1. INTRODUCTION

The early phases of the formation of a star are characterized by the presence of bipolar outflows, which, as the material falls onto the young star, eject matter at high speeds (several tens of km s^{-1}) to distances up to tens of parsec away (e.g., Arce et al. 2007). These outflows have a great impact on the surrounding gas. They can clear out cavities in their natal molecular clouds, and may eventually cause cloud disruption. As they propagate through molecular clouds, they create shock waves that compress, heat up and alter the chemical composition of the gas. Theoretical studies of shock waves in the interstellar medium (ISM; see Draine & McKee 1993 for a review) predict that their nature depends on the shock velocity and the intensity of the magnetic field. Slow shocks ($\leqslant$45 km s^{-1} for typical values of the magnetic field) are of type C: the density, temperature, and other quantities vary continuously through their passage. Furthermore, they are nondissociative: molecules generally survive their passage, although the chemical composition of the gas can be significantly altered. On the other hand, faster shocks produce discontinuities in both the density and temperature of the gas, and may dissociate molecules on their passage.

Observations of H_2 pure rotational lines in shock regions can provide important constraints on the physical and chemical conditions that prevail in these regions. For example, the H_2 ortho-to-para ratio (hereinafter *opr*) is predicted to be greatly affected by the passage of a C-type shock. In the cold (preshock) gas, H_2 is expected to be mostly in para form (Flower et al. 2006; Maret & Bergin 2007). In the shocked gas, reactive collisions with H atoms can convert p-H_2 into o-H_2 (Timmermann 1998; Wilgenbus et al. 2000). This reaction has a relatively high activation barrier ($\sim$4000 K), and therefore the efficiency of the conversion depends critically on the temperature that is reached in the shock. Indeed, Wilgenbus et al. (2000) showed that effective para to ortho H_2 conversion takes place in the temperature interval 700–1300 K, while Kristensen et al. (2007) refined this result in to the interval 800–3200 K. In addition, the efficiency of the conversion depends on the abundance of H atoms in the gas. Fast shocks produce higher H abundances, which makes the conversion faster.

Molecular hydrogen rotational lines have been observed in several star-forming regions with the *Infrared Space Observatory* (*ISO*) and, more recently, with the *Spitzer Space Telescope* (Werner et al. 2004). Using the Short Wavelength Spectrometer (SWS) on board *ISO*, Neufeld et al. (1998) observed five pure

[9] Current address: Laboratoire d'Astrophysique de Grenoble, Observatoire de Grenoble, Université Joseph Fourier, CNRS, UMR 571, BP 53, F-38041 Grenoble, France.

rotational lines (from $0-0\,S(1)$ to $0-0\,S(5)$, hereafter simply referred as $S(1)$ and $S(5)$, respectively) toward the Herbig-Haro 54 outflow (HH 54). Using these multiple ortho and para lines, they determined simultaneously the rotational temperature and the *opr*. Interestingly, they measured an *opr* of 1.3, which is significantly lower than the equilibrium value (∼3) at the observed gas temperature (∼650 K). Lefloch et al. (2003) used the ISOCAM camera to map the H_2 $S(2)$–$S(7)$ toward the HH 2 outflow, and found important spatial variations in the *opr* (between 1.2 and 2.5) around the HH 2 object. Neufeld et al. (2006) used the infrared spectrometer (IRS; Houck et al. 2004) on board *Spitzer* to map the *opr* toward HH 54 and HH 7-11, and also observed a low, nonequilibrium *opr*, with important spatial variations. The fact that the *opr* is out-of-equilibrium suggests that the ortho-to-para conversion is relatively slow in these regions: the observed *opr* was interpreted as a fossil of an earlier epoch when the gas was cooler.

This paper presents complete 5.2–36.5 μm spectral maps obtained with the IRS toward the NGC 1333 region in the Perseus cloud. The observations cover a region of roughly $6' \times 10'$, i.e., 0.4 pc × 0.5 pc assuming a distance of 220 pc (Cernis 1990). To our knowledge, these are the largest complete spectral maps obtained with the IRS. NGC 1333 contains many YSOs, revealed by submillimeter (Sandell & Knee 2001), millimeter (Lefloch et al. 1998), and mid-infrared continuum maps (Gutermuth et al. 2008). It also contains numerous molecular outflows, detected for example in CO line emission (Knee & Sandell 2000). Here, we focus on H_2 pure rotational line emission, from $S(0)$ to $S(7)$. These lines are used to map the H_2 rotational temperature and *opr* over a large region, thus permitting detailed study of the impact of outflows on the surrounding cloud. The paper is organized as follows. In Section 2, we present the observations and discuss the data reduction. The spectra and maps that we obtained are presented in Section 3. In Section 4, we describe the analysis procedure that we used to derive the H_2 column density, rotational temperature, and *opr* from our observations. In Section 5, we compare our observations with the predictions of shock models, we compare the variation of the *opr* with the temperature, and we discuss the impact of the outflows on the cloud. Our conclusions are presented in Section 6.

2. OBSERVATIONS

NGC 1333 was observed using the IRS during Cycle 2 of the General Observer program, in 2006 March and September. The long-high (LH), short-high (SH), and short-low (SL) modules of the IRS were used, providing a complete spectral coverage from 5.2 to 36.5 μm. The spectral resolution of these observations ($R = \lambda/\Delta\lambda$) ranges from 64 to 128 for the SL mode, and is ∼600 for the high-resolution modules (SH and LH). The half-power beam size of the instrument ranges from 3″ at 5.2 μm to 10″ at 38 μm (Neufeld et al. 2006).

The SH observations consist of nine different Astronomical Observations Requests (AORs), each covering a rectangular region of ∼142″ × 120″. Each of these AORs was obtained by moving the IRS slit in both perpendicular and parallel directions of the slit length, with a half-slit width stepping in the perpendicular direction, and full-slit length in the parallel direction. Our SH observations do not cover the tip of the HH 7-11 outflow; therefore, we have used archival data of this region obtained in 2004 February as part of the IRAC Guaranteed Time program, and that consists of two AORs of 58″ × 76″ each. Details on these data can be found in Neufeld et al. (2006). When merged, the SH AORs cover a region of $\sim 6' \times 10'$, roughly centered on SVS 13 ($\alpha = 17^h22^m38^s.2$ and $\delta = -23°49'34''.0$; J2000). The LH observations consist of six AORs of ∼200″ × 273″ each. As for the SH observations, these were obtained with a half-slit width stepping in the perpendicular direction, and full-slit length in the parallel direction. These observations cover a region of $\sim 8' \times 9'$. Finally, the SL observations consist of six AORs of ∼202″ × 222″, each obtained with a full-slit width stepping in the perpendicular direction, and half-slit width stepping in the parallel direction. These observations cover a region of $\sim 6' \times 14'$.

All the data, including the archival ones, have been reduced using the latest version (17.2) of the *Spitzer* Science Center pipeline. Further reduction was performed using the SMART software package (Higdon et al. 2004), supplemented by the IDL routines described in Neufeld et al. (2006). These routines remove the bad pixels in the LH and SH observations, extract spectra for each pixel along the slit of the different modules, spatially resample the spectra on a regular grid (with a spatial resolution corresponding to the pixel spacing, i.e., 2″.3, 1″.8 and 4″.5 for the SH, SL, and LH modes, respectively), and finally produce continuum-subtracted spectral maps by fitting a Gaussian for each spectral line. A first look at our LH and SH spectral maps revealed the presence of stripes in the direction perpendicular to the slit length. As discussed in Neufeld et al. (2007), these stripes are due to the bad pixel extraction routine, which interpolates missing pixel values in the dispersion direction. Therefore, if a bad pixel is close to the central wavelength of a given line, the intensity measured at a given position along the slit is consistently underestimated, creating the observed stripes. Following Neufeld et al. (2007), we have corrected this effect by applying a correction factor for each line and each position along the slit (see Neufeld et al. 2007 for details on how this correction factor is determined). This technique was found to remove the stripes from our maps quite efficiently. Note that our LH observations were not affected by this problem because they were obtained with a half-slit length stepping in the parallel direction, as opposed to the SH and SL data which were obtained with a full-slit length stepping in that direction. Therefore, in LH mode, any given position on the sky was observed twice, and potential stripes were washed out when averaging the spectra together.

3. RESULTS

3.1. Spectra

Figures 1–3 present average spectra obtained on several positions of our maps. These spectra were obtained by averaging all the spectra observed within a 15″ FWHM Gaussian aperture around a given position, in order to increase the signal-to-noise ratio. We detect eight pure rotational lines—from $S(0)$ to $S(7)$—toward HH 7. On the other hand, no H_2 emission is detected toward the NGC 1333–IRAS 4A and 4B Class 0 protostars. Several fine structure atomic lines are also detected, such as the Fe II $^4F_{7/2} - ^4F_{9/2}$ (17.9 μm), the S I $^3P_1 - ^3P_2$ (25.2 μm), Fe II $^6D_{7/2} - ^6D_{9/2}$ (26.0 μm), and Si II $^2P^0_{3/2} - ^2P^0_{1/2}$ (34.8 μm) lines. Table 1 gives the intensities measured toward several positions for these lines. Thanks to an overlap in the wavelength range covered by the SL and SH modules, the H_2 $S(2)$ intensity was measured with each module, and was found to agree within ∼20%.

Several polycyclic aromatic hydrocarbon (PAH) features—at 6.2, 7.2, 8.6, 11.2, and 12.8 μm—as well as the 9.7 μm

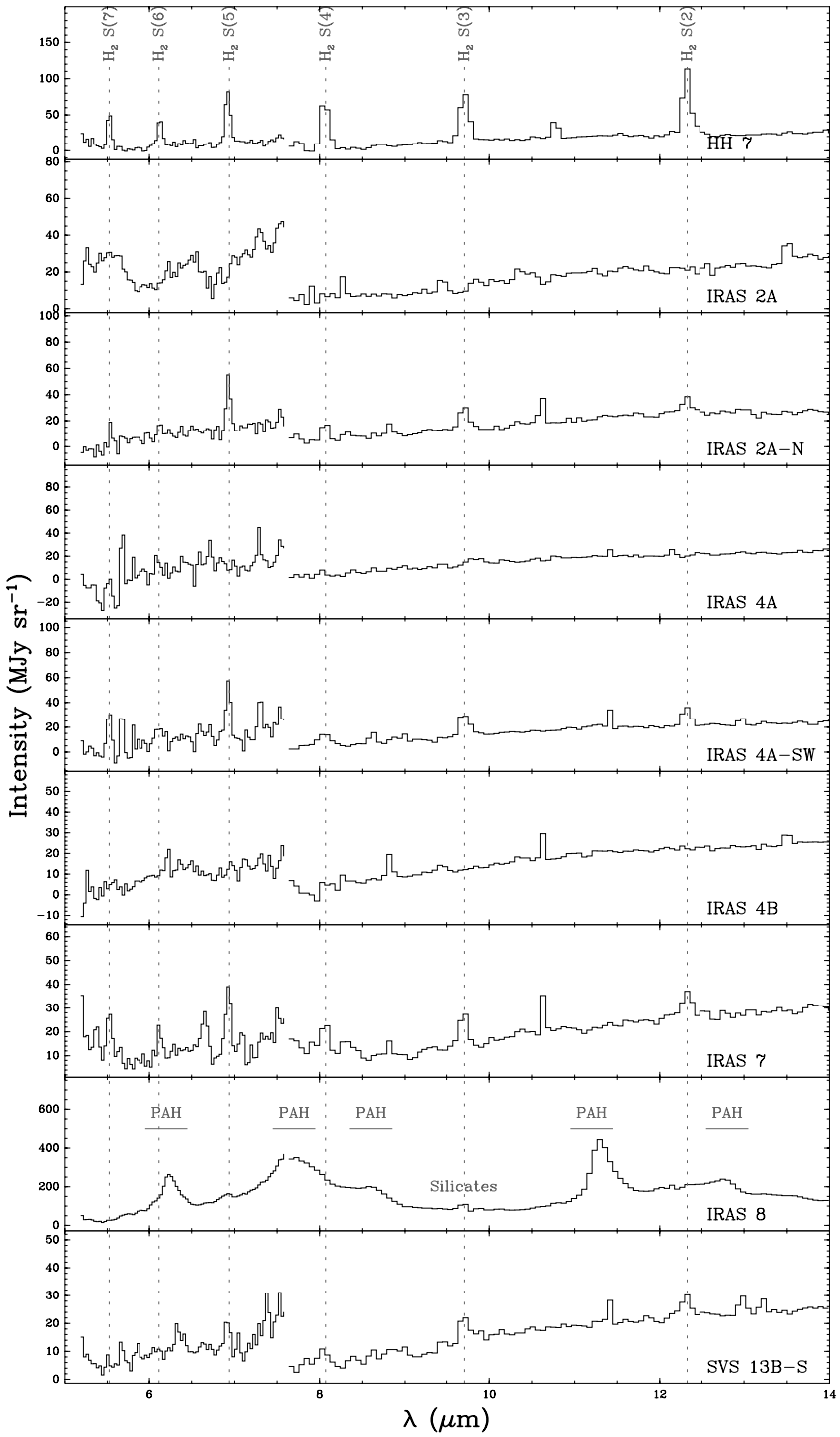

Figure 1. Averaged spectra observed with the SL module for 15″ Gaussian apertures centered, from top to bottom, on HH 7 ($\alpha = 03^{h}29^{m}08^{s}.45$, $\delta = +31°15'29''.2$; J2000) IRAS 2A ($\alpha = 03^{h}28^{m}55^{s}.59$, $\delta = +31°14'37''.3$; J2000), IRAS 2A-S ($\alpha = 03^{h}28^{m}54^{s}.04$, $\delta = +31°13'31''.2$; J2000), IRAS 4A ($\alpha = 03^{h}29^{m}10^{s}.29$, $\delta = +31°13'31''.8$; J2000), IRAS 4A-SW ($\alpha = 03^{h}29^{m}06^{s}.62$, $\delta = +31°12'17''.7$; J2000), IRAS 4B ($\alpha = 03^{h}29^{m}11^{s}.99$, $\delta = +31°13'08''.9$; J2000), IRAS 7 ($\alpha = 03^{h}29^{m}11^{s}.31$, $\delta = +31°18'31''.1$; J2000), IRAS 8 ($\alpha = 03^{h}29^{m}12^{s}.5$, $\delta = +31°22'08''$; J2000), and SVS 13B-S ($\alpha = 03^{h}29^{m}05^{s}.0$, $\delta = +31°13'14''$; J2000). Pure rotational H_2 transitions are indicated, as well as the 6.2, 7.2, 8.6, 11.2, and 12.8 μm PAH features, and the 9.7 μm silicates absorption band. The spectra between ~5 and 7.5 μm and between ~7.5 and 14 μm correspond to the second and first order of the module, respectively.

silicates absorption band are clearly detected toward IRAS 8. Finally, the CO_2 ice feature at 15.2 μm is seen on IRAS 2. A discussion of all the detected spectral features is beyond the scope of this paper; in the following, we focus on the interpretation of the H_2 line emission, and we postpone the discussion of other lines and spectral features to forthcoming papers.

3.2. Maps

Figures 4(a)–(i) show maps of the H_2 $S(0)$–$S(7)$ lines. $H_2S(1)$, $S(2)$, $S(3)$, $S(4)$, and $S(5)$ emission is readily detected along several outflows. The H_2 $S(0)$, $S(6)$, and $S(7)$ maps have a lower signal-to-noise ratio, and emission of these lines is barely detected at this spatial resolution (4″.5 and 1″.8 for the LH

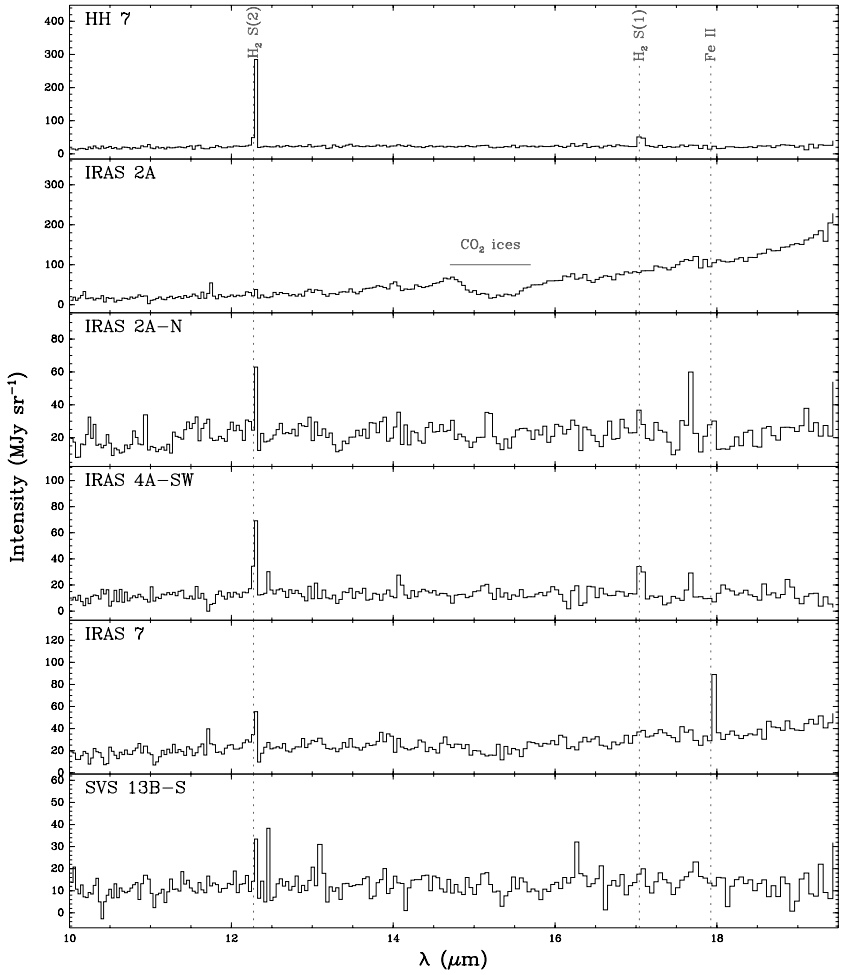

Figure 2. Same as Figure 1 for the SH module. The position of the 15.2 $\mu$$CO_2$ ice feature is indicated. For clarity the spectral resolution has been degraded by a factor of 4.

Table 1
Line Intensities

Transition	Wavelength	Module	Intensity (10^{-5} erg cm^{-2} s^{-1} sr^{-1})				
	(μm)		HH 7	IRAS 4A-SW	IRAS 2A-N	IRAS 7	SVS 13B-S
H_2 $S(0)$	28.2188	LH	0.45	0.30	0.14	0.25	0.17
H_2 $S(1)$	17.0348	SH	2.82	2.02	1.08	0.89	0.75
H_2 $S(2)$	12.2786	SH	21.28	4.79	3.66	2.88	2.05
H_2 $S(3)$	9.6649	L1	28.75	8.85	7.39	6.05	3.16
H_2 $S(4)$	8.0251	L1	39.35	8.04	12.31	11.24	3.63
H_2 $S(5)$	6.9095	L2	35.86	22.94	17.25	13.13	5.82
H_2 $S(6)$	6.1086	L2	21.94	14.24	4.54	5.50	<2.94[a]
H_2 $S(7)$	5.5112	L2	31.31	21.63	7.06	13.81	5.54
Fe II $^6D_{7/2}$ $-^6D_{9/2}$	25.9882	LH	0.71	0.49	0.22	3.34	0.26
S I $^3P_1$ $-^3P_2$	25.2490	LH	0.62	0.38	1.71	0.38	0.32
Si II $^2P^0_{3/2}$ $-^2P^0_{1/2}$	34.8141	LH	1.01	0.39	0.20	3.24	0.41

Note. [a] 1σ upper limit.

and SL modes, respectively). In the following, we discuss the morphology of the H_2 emission along the different outflows.

3.2.1. SVS 13 and HH 7-11

The Class I source SVS 13 (Strom et al. 1976) is associated with a chain of Herbig-Haro objects, HH 7-11. These objects are excited by a high-velocity molecular outflow, which is detected in CO and SiO rotational lines (Bachiller et al. 1998a, 2000; Knee & Sandell 2000), as well as the H_2 $1-0$ $S(1)$ rovibrational line at 2.12 μm (Aspin et al. 1994; Hodapp & Ladd 1995; Khanzadyan et al. 2003). A second outflow, roughly orientated along a north–south axis and driven by the SVS 13B Class 0 source, is detected in SiO $J = 2-1$ emission (Bachiller et al. 1998b).

The south–east lobe of the HH 7-11 outflow is clearly detected in our $S(1)$ map (Figure 4(a)). This map does not cover the north–

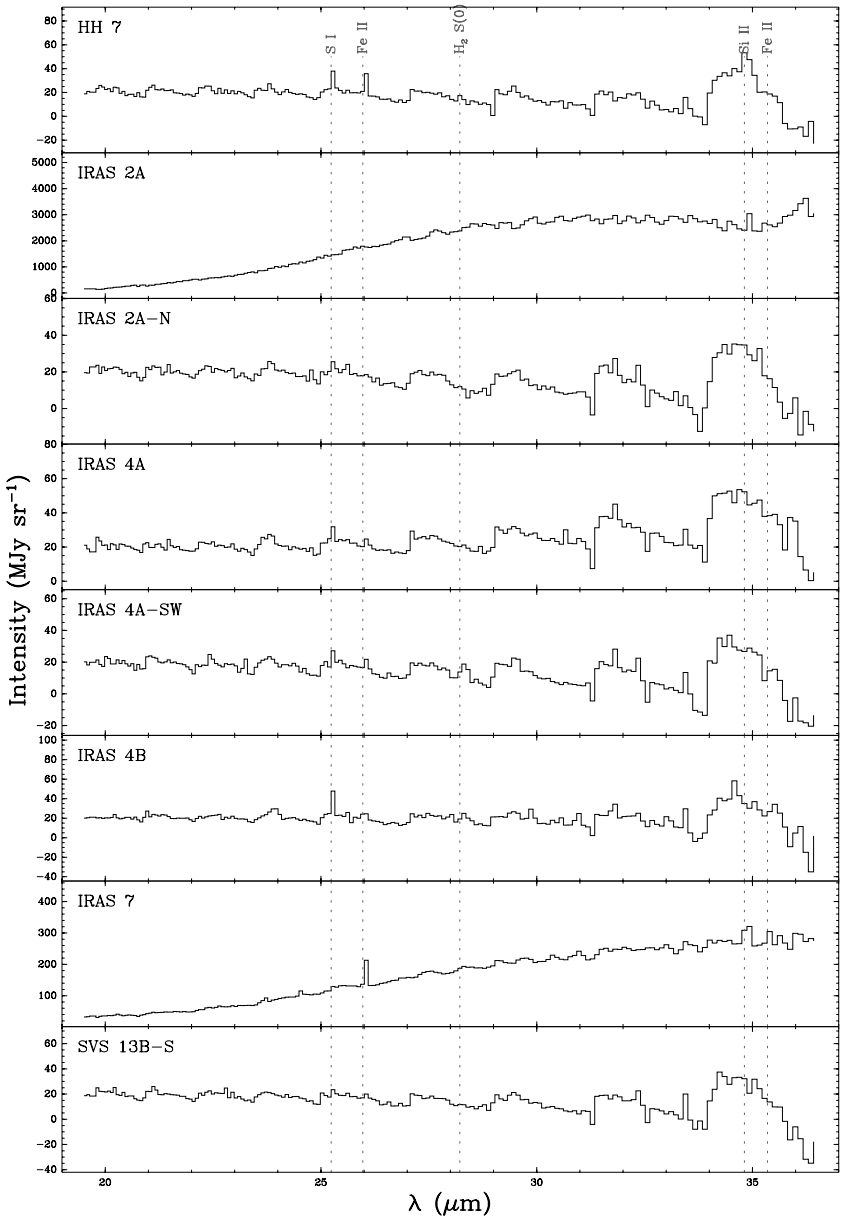

Figure 3. Same as Figure 1 for the LH module. For clarity the spectral resolution has been degraded by a factor of 4. The steps seen in some of these spectra are caused by offsets in response of the different orders of the module.

west lobe, but emission from this lobe is seen in the $S(2)$ and $S(3)$ maps (Figures 4(b) and (c)). H_2 $S(1)$ and $S(3)$ emission is also detected along the north–south outflow originating from SVS 13B. The position angle (from the north to east) of the H_2 emission is about 160°. The emission extends as far as ∼3′ south of SVS 13B, up to the tip of the NGC 1333–IRAS 4A outflow (see below). Some weak emission along this flow is also seen in the H_2 $S(2)$ line. Diffuse $S(1)$ emission extends to the north along the same axis, and may be associated with this outflow as well (see Section 3.2.5).

3.2.2. NGC 1333–IRAS 2

NGC 1333–IRAS 2 (Jennings et al. 1987, hereafter IRAS 2) is a binary system composed of the IRAS 2A and IRAS 2B Class 0 protostars. This system is associated with two outflows that both originate ∼6″ west of IRAS 2A (Knee & Sandell 2000). The first one is roughly orientated along a north–south axis, and is detected in CO (Liseau et al. 1988; Sandell et al. 1994) and H_2 $1-0$ $S(1)$ (Hodapp & Ladd 1995). The second outflow is roughly oriented along an east–west axis (position angle ∼104°) and is detected in CO, CH_3OH, and SiO (Sandell et al. 1994; Bachiller et al. 1998a; Knee & Sandell 2000; Jørgensen et al. 2004).

In our maps, we observe a peak of $S(1)$, $S(2)$, and $S(3)$ emission east of IRAS 2B along the axis of the east–west outflow. The position of this peak corresponds to the peak of the CS and CH_3OH emission, and presumably arises from a bow shock (Langer et al. 1996; Bachiller et al. 1998a). No emission is seen west of the source, but our maps have limited coverage in that direction. Two H_2 emission spots are also seen north and south of IRAS 2A. These two peaks lie at a position angle of ∼12°, consistent with the orientation of the H_2 $1-0$ $S(1)$ jet, but slightly different from the position angle of the CO jet (∼25° Sandell et al. 1994). No emission is seen toward the protostars.

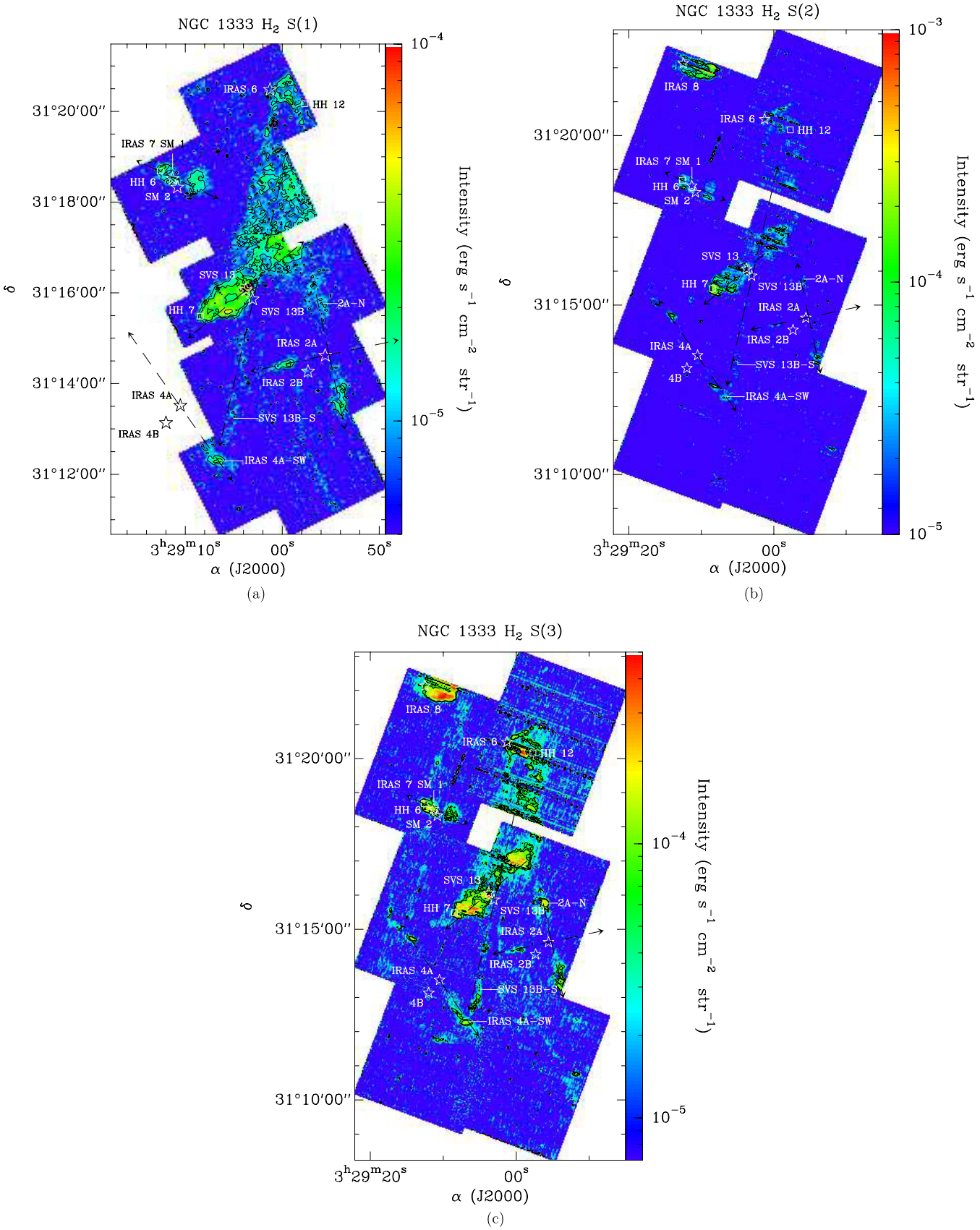

Figure 4. (a) H_2 $S(1)$ continuum-subtracted map obtained with the SH module. YSOs are indicated by open stars, while several HH objects are indicated by open squares. The outflows discussed in the text are indicated by the dashed arrows. The two positions along the IRAS 2 and IRAS 4A outflows that are discussed in the text, IRAS 2A-N and IRAS 4A-SW, are also shown. Contours show the 3σ, 5σ, and 10σ noise levels. (b) H_2 $S(2)$ map obtained with the SL module. Contours show the 3σ and 5σ noise level. (c) H_2 $S(3)$ map obtained with the SL module. Contours show the 3σ and 5σ noise level.

(An extended color version of this figure is available in the online journal.)

3.2.3. NGC 1333–IRAS 4

NGC 1333–IRAS 4 is also a binary system, composed of two Class 0 protostars, IRAS 4A and IRAS 4B. IRAS 4A drives a powerful and well-collimated outflow that extends roughly over 4′, and is detected in H_2 $1-0$ $S(1)$ (Hodapp & Ladd 1995) as well as CO and SiO lines (Blake et al. 1995; Knee & Sandell 2000). A more compact outflow, with an inclination close to 90° (i.e., almost perpendicular to the plane of the sky), is driven by IRAS 4B (Blake et al. 1995).

We detect H_2 $S(1)$ emission at the southwestern tip of the IRAS 4A outflow. Unfortunately, our SH maps do not cover other parts of the flow. However, $S(2)$ and $S(3)$ emission peaks are seen at the north–east and south–west of IRAS 4A. No H_2 is detected from the IRAS 4B outflow, nor from IRAS 4A and IRAS 4B protostars themselves.

3.2.4. NGC 1333–IRAS 7 and HH 6

NGC 1333–IRAS 7 is associated with two submillimeter sources, SM 1 and SM 2 (Sandell & Knee 2001). The former is coincident with the centimeter source VLA 27 (Rodríguez et al. 1999), as well as with a water maser (Henkel et al. 1986). A molecular outflow, oriented along a east–west axis and probably driven by SM 1, is detected in CO (Liseau et al. 1988; Knee & Sandell 2000). This outflow is the driving source for the chain of HH objects located east of SM 1, which include HH 6. Our maps reveal bipolar H_2 emission orientated along the same axis as the CO outflow.

3.2.5. NGC 1333–IRAS 6 and HH 12

NGC 1333–IRAS 6 is coincident with a PMS star (SVS 107) and the continuum centimeter source VLA 42 (Rodríguez et al. 1999). An elongated structure is also seen toward that source in the submillimeter maps of Sandell & Knee (2001). West of NGC 1333–IRAS 6 is a chain of HH objects that include HH 12. Knee & Sandell (2000) suggested that these objects are excited by the outflow originating from SVS 13B.

In our H_2 maps, we see some diffuse emission west of IRAS 6 that extends from the south down to the north-west lobe of the SVS 13 outflow. Although this diffuse emission appears broadly aligned with the axis of the SVS 13B, it is difficult to say from the present data if the H_2 emission arises in the shocked gas from this outflow.

3.2.6. NGC 1333–IRAS 8

NGC 1333–IRAS 8 is part of the optical nebulosity north of the cloud (see Figure 4(b)). It is associated with a PMS star, SVS 3. Although the IRS spectrum is dominated by PAH features (see Figure 1), we also detect extended H_2 $S(2)$, $S(3)$, and $S(5)$ (but no $S(4)$) to the southeast of the source.

4. ANALYSIS

4.1. Rotational Diagrams

In Figure 5, we show rotational diagrams obtained for 15″ FWHM Gaussian apertures centered at several positions along the outflows: HH 7, IRAS 4A-SW, IRAS 2A-S, IRAS 7, and SVS 13B-S. These positions are indicated on the H_2 maps (Figures 4(a)–(i)). Line intensities were corrected for extinction using the standard ($R_v = 3.1$) galactic dust opacity curve from Weingartner & Draine (2001), assuming $A_v = 2$ for all sources (the value measured toward HH 8; Gredel 1996). In each diagram and for each line, we have plotted $\ln(N_u/(g_u g_s))$, where

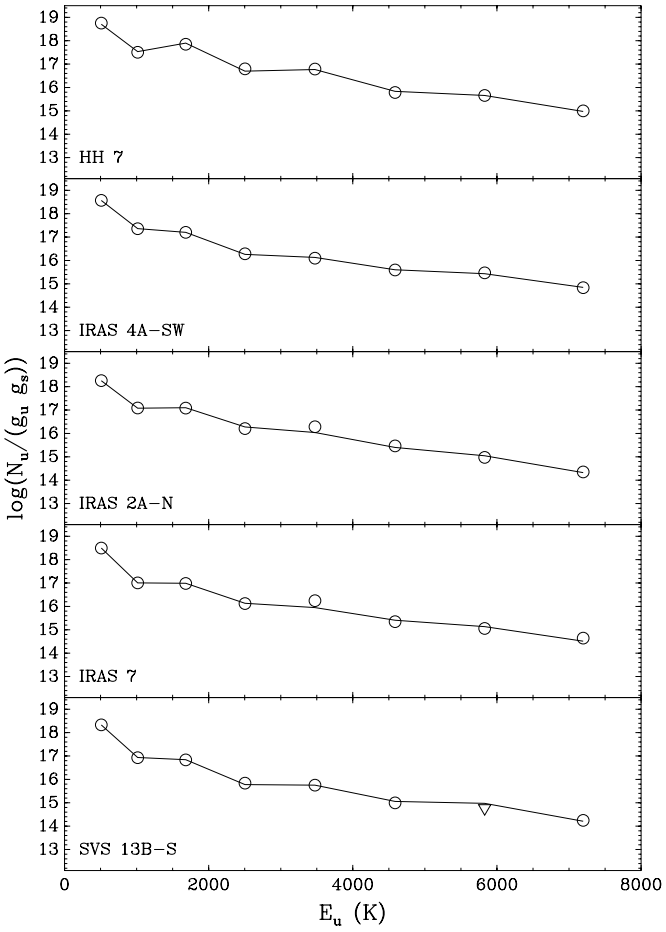

Figure 5. H_2 rotational diagrams obtained for 15″ Gaussian apertures centered on HH 7, IRAS 4A-SW, IRAS 2A-S, IRAS 7, and SVS 13B-S. The black open circles correspond to the observations. The black open triangle is a 1σ upper limit. The black solid lines are rotational diagram obtained assuming that two gas components, a warm and a hot one, are present (see Section 4.1).

N_u is the column density in the upper level, g_u is the rotational degeneracy (equal to $2J + 1$) and g_s is the spin degeneracy (three for ortho, and one for para transitions). If the *opr* is equal to its high temperature limit (i.e., 3), and if H_2 transitions are thermalized at a single temperature, then the observed values would line up on a straight line. Instead, the diagram show a "zig-zag" pattern, indicating that the *opr* is lower than 3. In addition, the rotational diagrams show a positive curvature; the observed values cannot be fitted with a single excitation temperature. This suggests that the observed H_2 emission arises in a mixture of gas with different temperatures, as already observed in HH 7 and HH 54 by Neufeld et al. (2006). Following these authors, we have fitted the observations with two gas components (herein after the "warm" and the "hot" components). Note that this two temperature model is an approximation; the gas has more likely a continuous temperature distribution. The total H_2 column density, *opr*, and excitation temperature in each gas component were kept as free parameters, and were adjusted to fit the observations using a minimization routine. These three parameter can be constrained quite independently from each other. The *opr* is constrained from the "zig-zag" pattern in the rotational diagram. The rotational temperature is determined from the slope of the rotational diagram. Finally, the total H_2 column density is determined from the ordinate of the points in the diagram. This procedure produced good fits to the data;

Table 2
Rotational Diagrams Results

Source	Warm Component			Hot Component		
	$N(H_2)$ (cm^{-2})	T_{rot} (K)	*opr*	$N(H_2)$ (cm^{-2})	T_{rot} (K)	*opr*
HH 7	5.9×10^{19}	611	0.37	6.2×10^{18}	1401	1.99
IRAS 4A-SW	5.9×10^{19}	342	0.69	3.4×10^{18}	1513	1.94
IRAS 2A-N	2.0×10^{19}	371	0.33	5.6×10^{18}	1055	2.09
IRAS 7	4.2×10^{18}	300	0.31	3.3×10^{18}	1268	2.11
SVS 13B-S	3.2×10^{19}	312	0.51	1.5×10^{18}	1337	1.43

in particular, no clear departures from the local thermodynamic equilibrium (LTE) is seen, even for the highest energy lines. The critical densities—above which collisional excitation dominates over radiative de-excitation, and energy levels are populated according to Boltzmann's statistic—range between 5 and 4×10^5 cm^{-3} for the $S(0)$ and $S(7)$ lines, respectively (assuming a kinetic temperature of 1000 K; Le Bourlot et al. 1999). Therefore the highest energy lines ($S(6)$ and $S(7)$) must arise in relatively dense gas ($>10^5$ cm^{-3}).

The best-fit parameters for HH 7, IRAS 4A-SW, IRAS 2A-S, IRAS 7, SVS 13B-S are given in Table 2. The rotational temperature toward these sources is between ~300 and ~600 K for the warm component, and ~1000–1500 K for the hot component. We measure an *opr* of 0.3–0.7 and 1.4–2.1 in the warm and hot components, respectively.[10] For both components, the *opr* is much lower than its equilibrium value for the measured (rotational) gas temperatures; for kinetic temperatures higher than 300 K, the equilibrium value is essentially 3. For all sources, we measure a higher *opr* in the hot component than in the warm component. Similar behavior was noted previously by Neufeld et al. (2006, 2007). The dependence of *opr* on temperature is discussed in further detail below. The H_2 column densities are typically $\sim(2\text{–}6) \times 10^{19}$ cm^2 and $\sim(3\text{–}6) \times 10^{18}$ cm^2 in the warm and hot components, respectively. Thus, the column density of the hot component is more than an order of magnitude smaller than the column density of the warm component.

4.2. H_2 Column Density, Rotational Temperature, and Ortho-to-Para Ratio Maps

Thanks to their large spatial coverage, our observations essentially map the *opr*, rotational temperature, and column density of H_2 in the core of the NGC 1333 cloud. For this purpose, the H_2 line maps were resampled on a common grid with a 5″ spacing. Only regions of the sky that were observed with all three modules were considered. We then constructed a rotational diagram in each pixel of the resulting map. As mentioned above, the H_2 rotational emission arises from at least two gas components. With three free parameters for each component (column density, *opr*, and rotational temperature), we need at least six lines detected in a given pixel of the maps. In practice, few pixels in our maps meet this criterion. Therefore, when constructing the maps, only the H_2 $S(0)$ to $S(3)$ transitions were considered, which allows for greater spatial coverage of the region. Since the $S(0)$ to $S(3)$ line emission is dominated by the warm component (see Figure 5), the column density, *opr*, and rotational temperature derived using these lines correspond to that component.

[10] The best-fit parameters we obtain for HH 7 differ slightly from those reported by Neufeld et al. (2006) on the same source. The reason is that we used new data in addition to those of Neufeld et al. (2006).

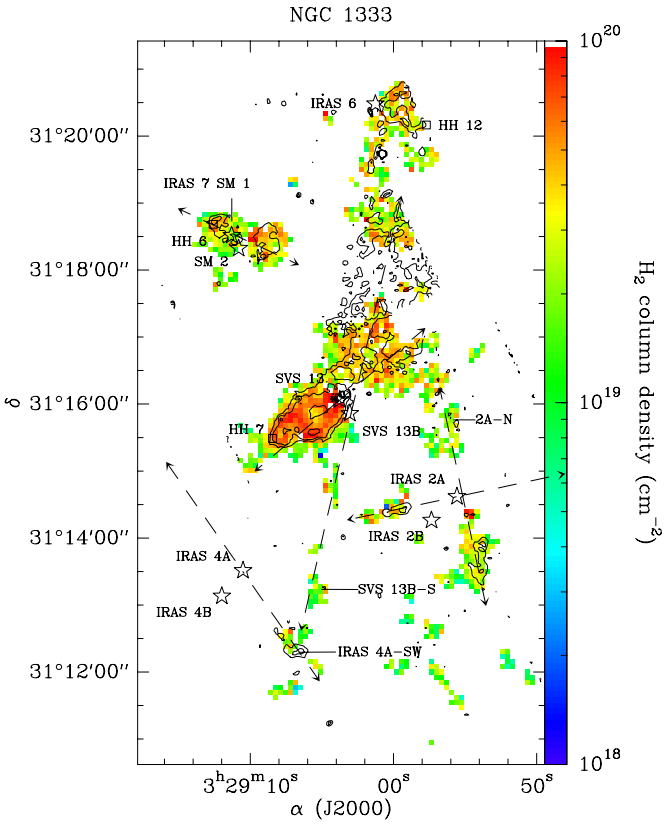

Figure 6. H_2 column density map (color points) on top of the H_2 $S(1)$ emission (black contours). Regions of the map that appear in white correspond to points where a rotational diagram could not be constructed because of missing data or insufficient signal-to-noise ratio. Contour levels are those of the $S(1)$ emission taken from Figure 4(a). Pixel size is 5″.

(A color version of this figure is available in the online journal.)

In Figures 6–8, we provide maps of the H_2 column density, rotational temperature, and *opr*. These quantities could be measured along both lobes of the SVS 13 outflow and around IRAS 7. We could also map those at the south–west tip of the IRAS 4A outflow, as well at the northern, southern, and western tips of the IRAS 2 outflows. Elsewhere in the map, we did not detect the H_2 $S(0)$, $S(1)$, $S(2)$, and $S(3)$ lines simultaneously, or the lines were detected with an insufficient signal-to-noise ratio. Where measured, some important variations in these quantities are seen. The H_2 column density ranges from 3×10^{18} to 10^{20} cm^{-2}. The highest column densities are seen along the HH 7-11 outflow (see Figure 6). The rotational temperature ranges between 200 and 650 K, with a maximum reached close to the position of HH 7, as well as the IRAS 2N position (see Figure 7). Finally, the H_2 *opr* ranges from 0.1 and 3 (Figure 8).

Some important variations in both the rotational temperature and the *opr* are seen. Along the HH 7-11 outflow, between SVS 13 and HH 8, we measure a rotational temperature of ~400 K and an *opr* ranging between 1.5 and 2. Around HH 7, we measure a higher rotational temperature (~650 K), but a lower *opr* (~0.5). The presence of hot gas with a low *opr* in front of the HH 7-11 has already been observed by Neufeld et al. (2006). They suggested that this gas has been compressed and heated up by the passage of the shock, but the *opr* has not reached LTE yet. Along the northwestern lobe of this flow, the spectra are noisier, and large variations from one pixel to the next. Around IRAS 4-SW, the rotational temperature and the *opr* were measured only in a few pixels making the comparison between

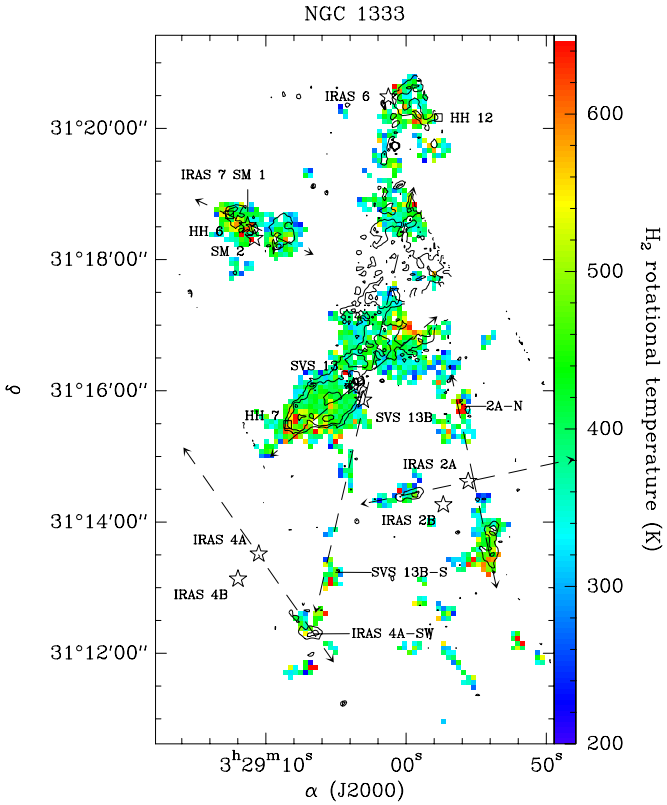

Figure 7. Same as Figure 6 for the H_2 rotational temperature.
(A color version of this figure is available in the online journal.)

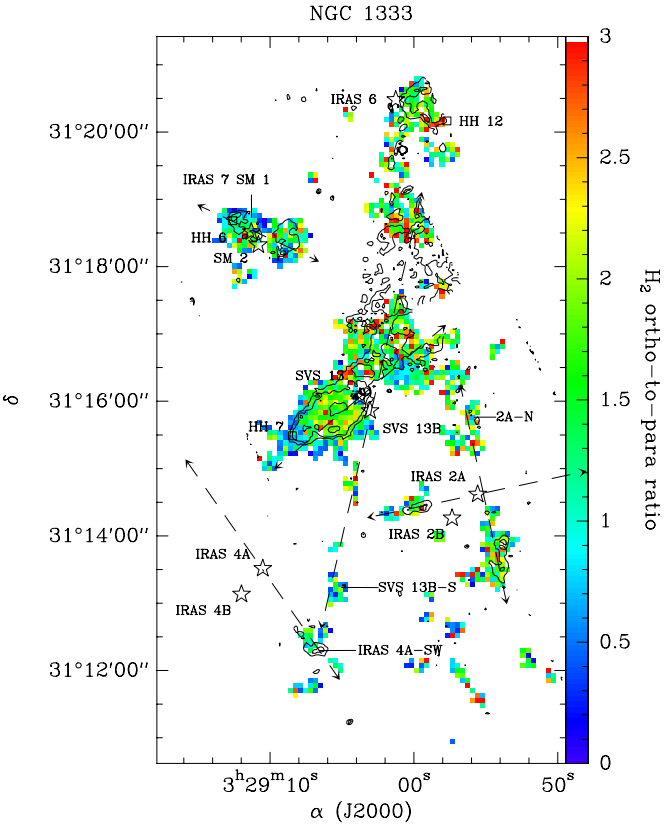

Figure 8. Same as Figure 6 for the H_2 *opr*.
(A color version of this figure is available in the online journal.)

these two quantities difficult. On the other hand, we observe some variation in the rotational temperature along the north and south lobes of the IRAS 2 outflow. Like in HH 7-11, the rotational temperature is higher at the tip of this outflow. However, no corresponding variation is seen in the *opr*. Some relatively hot gas (∼500 K) with a low *opr* (∼1) is also observed around the eastern lobe of the IRAS 7 outflow. The variation of the *opr* as a function of the $T_{\rm rot}$ is further discussed in the Appendix.

5. MODEL AND DISCUSSION

5.1. Comparison of the Observed Emission with the Predictions of a Shock Model

In this section, we compare the observed H_2 line emission toward several outflow positions with the predictions of a stationary, planar C-type shock model that includes ortho para interconversion (Flower & Pineau des Forêts 2003). The shock model has several free parameters: the preshock density n, the preshock velocity v, the initial (preshock) ortho-to-para ratio opr_i, and the intensity of the transverse magnetic field. The latter is expressed as $b = B_t\, n_0^{-1/2}$, where B_t is the transverse magnetic field in μG and n_0 is the preshock density in cm^{-3}. The model has been run for a grid of parameters (L. E. Kristensen et al. 2009, in preparation), and the results of these computations are available on the Web.[11]

In Figure 9, we compare the column densities obtained from our observations on aperture-averaged positions with those predicted by the shock model. As a first approach, we have tried to reproduce the observed column densities with a single component shock. The value of b was set to 1, and the other parameters of the model were adjusted until a good agreement with the observations was obtained. We found that the observed $S(0)$, $S(1)$, $S(2)$ emission were fairly well fitted for a preshock density of 10^4 cm^{-3}, an initial *opr* of 0.01 or 1, a preshock velocity of 12–24 km s^{-1}, and a beam filling factor ff of typically 10%. However, this model greatly underestimates the observed lines with higher energies. In other words, the temperature reached in a slow shock is not sufficient to explain the $S(3)$–$S(7)$ line that we observe. This emission requires higher gas temperatures that are reached only in faster shocks. Therefore, we have tried to match the observed column densities with a combination of slow and fast shock components. Both the preshock density and initial *opr* were kept the same as for the slow shock component, and the velocity of the fast shock component was adjusted in order to match the $S(3)$–$S(7)$ lines. We found that the emission of these lines were well matched for a shock velocity of 36–53 km s^{-1} and a filling factor of typically 1%. In fact, this two-component model provides an excellent fit to the observations (see Figure 5), with the exception of the $S(0)$ line ($E_{\rm up}$ = 510 K) in IRAS-2, IRAS-7, and SVS13B-S, which is somewhat underestimated by the model. Possibly, this line arises in a separate, nonshock component toward these sources. Indeed, in their study of supernovae remnants, Neufeld et al. (2007) found that the $S(0)$ emission was more extended than other spectral lines they observed. In one source, they found evidence for both a shock excited $S(0)$ component and a diffuse emission component.

Table 3 gives the best-fit model parameters for the slow and fast shock components. Toward all positions, we obtain a good fit for a preshock density of 10^4 cm^{-3}. The shock velocity in the slow shock component is between 12 and 24 km s^{-1}, while that

[11] http://www.strw.leidenuniv.nl/∼kristensen/models

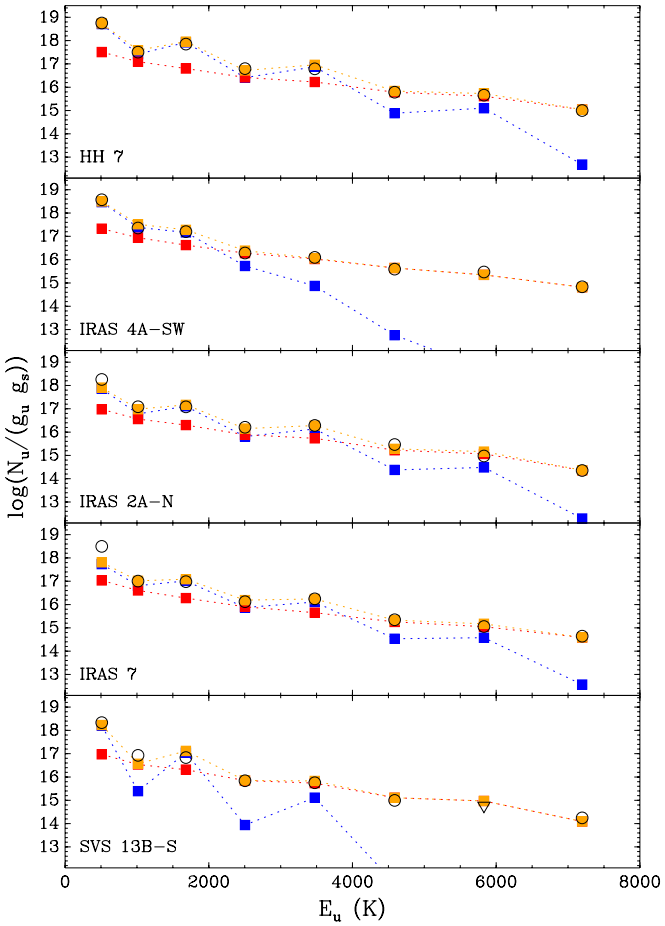

Figure 9. Same as in Figure 5, but with the two velocity components shock model predictions over plotted (see Section 5.1). The blue and red squares connected by the dotted lines show the emission from the slow and fast shock components, respectively. The orange squares connected by the dotted lines show the total emission from these two components. Note that some of the blue squares (at low energies) as well as some of the red squares (at high energies) are masked by the orange squares.

(A color version of this figure is available in the online journal.)

in the fast shock component is between 36 and 53 km s^{-1}. For all sources but IRAS 4-SW, the emission is well matched assuming an initial *opr* of 0.01. For the latter, we obtain a slightly better fit for an initial *opr* of 1.0. However, the grid of models covers only a relatively small sample of opr_i (0.01, 1, 2, and 3) so this parameter is not constrained precisely. It is likely that opr_i values ranging between 0.01 and 1 would also provide a good fit to the observations. The filling factor ranges from 2% to 15% for the slow component, and from 0.8% to 3% for the fast component. Since shocks driven by a collimated jet are not planar but have a bow shape, it seems natural that we observe a range of velocities: at the apex of the bow, the shock is moving faster with respect to the wings of the bow (Smith et al. 1991). This high-velocity component has a small beam filling factor, because the high velocities are present only at the apex of the bow. On the other hand, slower gas—leading to lower excitation—is present in the broader wings of the bow.

It is worth noting that the fit is not be unique. For example, we found that the emission observed in HH 7 can also be fitted by a model with an higher preshock density (10^5 cm^{-3}), but a smaller preshock velocity (15 and 30 km s^{-1} for the slow and fast component, respectively). In this case, the observations require an initial *opr* of 1, because the para-to-ortho conversion

Table 3
Best-fit Shock Model Parameters for Aperture-averaged Positions

Source	Slow Shock Component				Fast Shock Component			
	n(H) (cm^{-3})	v (km s^{-1})	opr_i	ff (%)	n(H) (cm^{-3})	v (km s^{-1})	opr_i	ff (%)
HH 7	10^4	22	0.01	15	10^4	45	0.01	3
IRAS 4A-SW	10^4	12	1	12	10^4	41	1	2
IRAS 2A-S	10^4	23	0.01	4	10^4	50	0.01	1.5
IRAS 7	10^4	24	0.01	2.2	10^4	53	0.01	1.1
SVS 13B-S	10^4	14	0.01	3	10^4	36	0.01	0.8

at these shock velocities is not efficient enough. Another reasonable fit was found for a preshock density of 10^6 cm^{-3} and preshock velocities of 10 and 20 km s^{-1} for the slow and fast component, respectively. Therefore, the preshock density and the preshock velocity are difficult to constrain simultaneously from the present observations. However, other constraints on these parameters have been obtained using far-infrared (FIR) lines observations. Molinari et al. (2000) observed CO and H_2 lines with *ISO*, and compared these observations with the predictions of Kaufman & Neufeld (1996) shock models. They found that the observed emission was well reproduced by a shock with a velocity ranging between 15 and 20 km s^{-1}, and a preshock density of 10^4 cm^{-3}. Giannini et al. (2001) also compared the H_2O and CO line emission observed with the Long Wavelength Spectrometer (LWS) on board *ISO* towards the red lobe of the IRAS 4 outflow to the model predictions of Kaufman & Neufeld (1996). Their observations are consistent with a velocity ranging between 15 and 20 km s^{-1}, and a preshock density of 10^4 cm^{-3} (see their Figure 8). Thus, the preshock density adopted here is consistent with the values derived by these authors using CO emission, which is a much more sensitive probe of density. It is also interesting to note that the shock velocity range they obtain agree well with what we obtain here for the slow shock component. Furthermore, Smith et al. (2003) obtained images of the $2-1S(1)$ and $1-0S(1)$ H_2 emission lines around the HH 7 bow shock. They found that their observations were well reproduced by a C-type shock model with a preshock density of 8×10^3 cm^{-3}, a bow speed of 55 km s^{-1} and a magnetic field of 97 μG (corresponding to $b \simeq 1$ for that preshock density). These parameters agree remarkably well with the values obtained here. The bow speed is slightly higher than the velocity we derive for the fast shock component (45 km s^{-1}). This is consistent with models that predict that pure rotational H_2 lines arise in the wings of the bow, where the shock velocity is smaller than at the apex (see Smith et al. 2003, Figure 5).

An important result of the present study is that the H_2 observations cannot be reproduced by an initial *opr* greater than 1; models with $opr_i = 2$ or 3 produce "flat" rotational diagrams, i.e., *opr* values that are close to the high temperature limit of 3. This indicates that H_2 in the cold gas (i.e., before the passage of a shock) is mostly in para form. Flower et al. (2006) studied the evolution of the *opr* as a function of time in a prestellar core. In their computations, H_2 is assumed to form on the grains with an *opr* of 3. Reactive collisions between o-H_2 and p-H_3^+ (or o-H_3^+) forms p-H_2, and consequently the *opr* decreases with time. The steady-state value ($\sim 3 \times 10^{-3}$ for $T = 10$ K and $\sim 3 \times 10^{-2}$ for $T = 30$ K) is reached after $t \sim 3 \times 10^7$ yr, for a density of 10^4 cm^{-3}. Our observations and modeling suggest that the initial *opr* is lower than 1. According to the Flower et al. (2006) computations, an ortho-to-para of 1 is reached after 3×10^6 yr (see their Figure 1); this is comparable to the lifetime of

nearby molecular clouds obtained by Hartmann et al. (2001). Therefore, the value of the initial *opr* is consistent with that is expected from chemical models.

5.2. Thermal History of the Shocked Gas

The measure of the *opr* along the several outflows in the cloud provides constraints on the thermal history of the gas. Our observations and models suggest that in the cold gas, H_2 is mostly in para form. Shock waves heat up the gas and trigger para-to-ortho conversion by reactive collisions with H, so the *opr* increases. However, the reaction has a large activation barrier (∼3900 K), so it is only efficient for gas temperatures greater than a few thousand Kelvins. As the postshock gas cools down, the interconversion becomes less efficient, and the *opr* remains frozen. Of course, reactions with H_3^+ will tend to decrease the *opr* in the postshock gas. However, this occurs on relatively long timescales (∼10^6 yr for $n_H = 10^4$; Flower et al. 2006), when compared with the dynamical timescale of the flows. Thus, the *opr* retains a memory of the thermal history of the gas.

Constraints on the thermal history of the gas may be placed by simple considerations. If we assume that a parcel of the gas is warmed up by a passage of a shock wave to a temperature T for a duration τ, and that ortho–para interconversion occurs only by reactive collisions with H, then the fraction of H_2 in ortho form in this parcel is given by (Neufeld et al. 2006)

$$f_{\rm ortho}(\tau) = f^i_{\rm ortho} \exp\left(\frac{-n({\rm H})\, k\, \tau}{f^{\rm LTE}_{\rm ortho}}\right) + f^{\rm LTE}_{\rm ortho}\left[1 - \exp\left(\frac{-n({\rm H})\, k\, \tau}{f^{\rm LTE}_{\rm ortho}}\right)\right], \quad (1)$$

where $f^i_{\rm ortho}$ is the initial ortho fraction, $f^{\rm LTE}_{\rm ortho}$ is the ortho fraction at the LTE, n(H) is the hydrogen density, and $k = k_{\rm po} + k_{\rm op}$ is the sum of the rate coefficients for para-to-ortho and ortho-to-para conversion, given by $k = 10^{-11} \exp(-3900/T)$ cm^3 s^{-1} (Schofield 1967).[12] Following Neufeld et al. (2006), we assume that H in the shocked gas is mainly produced by the formation of water from atomic oxygen, so that $n({\rm H})/n(H_2) \sim 10^{-3}$. Thus, for a preshock H_2 density of 10^4 cm^{-3}, n(H) ∼ 10 cm^{-3}. Figure 10 shows the *opr* as a function of time for different gas temperatures, assuming an initial *opr* of 0.01. In HH 7, we measure an *opr* of 0.37 and 1.99 in the warm ($T = 611$ K) and hot ($T = 1401$ K) components, respectively. This corresponds to timescales of ∼8×10^3 and ∼$\times 10^3$ yr for the warm and hot components, respectively.

The values we obtain can be compared with the prediction of shock models. The timescale during which the gas temperature is elevated on passing through a nondissociative shock is given by $N_s/(n_0\, v_s)$, where N_s is the column density of the warm shocked gas, n_0 is the preshock density, and v_s is the preshock velocity (Neufeld et al. 2006). Assuming a preshock density of 10^4 cm^{-3}, and a preshock velocity of 20 km s^{-1}, we obtain, using the analytical expression for N_s from Neufeld et al. (2006), a shock timescale of 400 yr. This is about an order of magnitude lower than the timescales we obtain for both the warm and hot components of HH 7. This may suggest that several shocks waves have passed through the quiescent gas and have progressively increased the *opr*, so opr_i is greater than 0.01. If we assume that opr_i is 0.37—the value we observe in the warm component of HH 7, at the tip of the HH 7-11 outflow—we found, using Equation (1), that 800 yr are needed to reach the value of 1.99 measured in the hot component, assuming a temperature of 1401 K. This is broadly consistent with the 400 yr timescale obtain above.

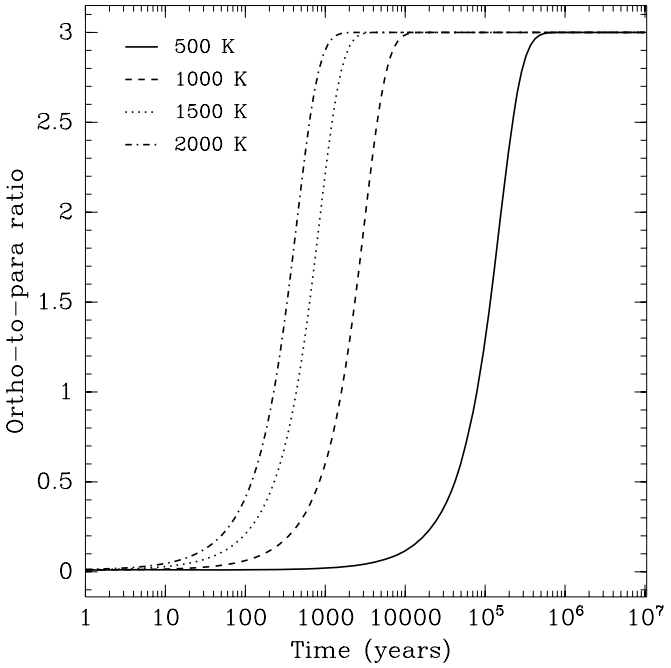

Figure 10. H_2 *opr* as a function of time for different gas temperatures. An initial *opr* of 0.01 and H density of 10 cm^{-3} are assumed for all curves.

5.3. Global Outflow Properties

We have obtained 5.2–35.8 μm spectroscopic maps encompassing nearly the full spatial extent of five molecular outflows from embedded young protostars (HH 7-11, SVS 13B, IRAS 4A, IRAS 2, IRAS 7). In the following section, we will explore how the information obtained in these maps provides a direct measurement of the mass loss rate and outflow energetics from these young stars.

5.3.1. Determination of Total Outflow Energy Loss

As shown in Figures 4(a)–(i), we have detected optically thin emission from eight rotational transitions of H_2 within these flows. Using these data, we can calculate the total H_2 luminosity in rotational emission, L_{H_2}, in the outflow by summing the emission over all rotational states and at each position within the region associated with each outflow. The transitions we have observed account for most of the luminosity carried by H_2 rotational emissions, the brightest transitions falling within the range with $J_{\rm up} = 2$–9 covered by *Spitzer*–IRS. We provide the value of L_{H_2} for each flow in Table 4. The H_2 luminosity is related to the total outflow cooling rate by $L_{\rm tot} = \frac{1}{f_c} L_{H_2}$, where f_c is the fraction of the total cooling due to H_2 rotational emissions.

The shock models of Kaufman & Neufeld (1996) can be used to explore the contribution of H_2 to the overall cooling of the outflow via emission. Based on analysis of the H_2 emission (Section 5.1) we find typical shock parameters of $n_0 \sim 10^4$ cm^{-3} and $v_s \sim$ 10–50 km s^{-1}. Under these conditions Kaufman &

[12] In the analogous equation given by Neufeld et al. (2006), $k_{\rm po}$, the rate coefficient for para-to-ortho conversion alone, was erroneously given in place of k. The former is 25% smaller than the latter (a difference which is negligible relative to other uncertainties).

Table 4
Outflow Properties

Source	L_{H_2} (10^{-2} $L_\odot$)	f_c	v_s (km s^{-1})	$\dot{M}_w$ ($M_\odot$ yr^{-1})	$\dot{P}$ ($M_\odot$ yr^{-1} km s^{-1})	τ_{dyn}[a] (yr)	P ($M_\odot$ km s^{-1})
HH 7-11	11.1	0.50	26	2×10^{-6}	5×10^{-5}	5600	0.29
IRAS 4A	1.8	0.25	16	2×10^{-6}	3×10^{-5}	12000	0.38
IRAS 2[b]	1.5	0.25	28	6×10^{-7}	2×10^{-5}	17000	0.34
IRAS 7	1.8	0.25	34	5×10^{-7}	2×10^{-5}	5700	0.11
SVS 13B	0.8	0.25	19	7×10^{-7}	2×10^{-5}	22000	0.44

Notes.
[a]From Knee & Sandell (2000).
[b]North–south outflow only.

Neufeld (1996) find that $f_c \sim 0.2$–0.7. The majority of H_2 cooling is via rotational lines, with only few percent contribution from H_2 vibrational emission. The rest of the cooling flux arises from rotational, and to a lesser extent vibrational, lines of H_2O and CO, along with [O I] fine structure emission.

The *ISO* has observed the primary cooling lines of CO, [O I], H_2O, OH, and H_2 with the SWS and LWS spectrometers in some of our sources. Molinari et al. (2000) observed HH 7 and compile the luminosities of the major cooling lines within the bandpass. For the HH 7 shock they find that 4.8×10^{-2} $L_\odot$ is released by O I, 2×10^{-2} $L_\odot$ by CO, 0.7×10^{-2} $L_\odot$ by H_2O, and 2.3×10^{-2} $L_\odot$ by H_2. However, the O I, CO, and H_2O observations were obtained using the LWS instrument with an 80″ beam centered on HH 7, while the H_2 observations covered only the $S(1)$–$S(5)$ transitions within a 14″ × 20″ SWS beam. Our observations in Figures 4(a)–(i) demonstrate that the H_2 emission extends well beyond the SWS aperture and the *ISO* SWS value is therefore a lower limit. We have convolved our data with a simulated 80″ LWS beam and have recomputed the total luminosity of H_2 from $S(0)$ to $S(7)$. We find that the H_2 luminosity in an 80″ beam centered on HH 7 is 0.1 $L_\odot$. Note that in this source, the luminosity of the H_2 $1-0S(0)$ rovibration line is 3×10^{-4} $L_\odot$ (Khanzadyan et al. 2003), well below the H_2 luminosity in rotational emission. Combining the *ISO* observations with this revised value, we find that the H_2 provides about 50% of the total cooling ($f_c \sim 0.5$), in good agreement with models.

Information for other flows can be gleaned from the summary of *ISO* cooling lines of Giannini et al. (2001) which included two of our sources: the IRAS 2 north–south flow, and the IRAS 4A outflow. For these sources, we find (after adapting the results of Giannini et al. to our adopted distance of 220 pc) that $f_c \sim 0.25$. Using this information the total cooling luminosity of the outflows in NGC 1333 is approximately $L_{tot} \sim 2$–4 L_{H_2}. For HH 7-11, we will adopt a $f_c = 0.5$ and for all other flows (which are not as prominent as HH 7-11) we adopt $f_c = 0.25$.

5.3.2. Determination of the Stellar Mass Loss by Outflows

The total energy loss generated by the outflow driven shock determined above is a direct measurement of the mechanical luminosity of the outflows. In this fashion, $\frac{1}{2}\dot{M}_o v_s^2 = (1 - f_m)L_{tot} = (1-f_m)\frac{1}{f_c}L_{H_2}$, where $(1-f_m)$ is the fraction of shock mechanical energy that is translated into internal excitation, as opposed to translational motion. Kaufman & Neufeld (1996) estimate that $(1 - f_m) \sim 0.75$ and we can then use the H_2 cooling emission to determine the outflow mass loss rate, $\dot{M}_o$ from the young star. This equation can be simplified and placed in terms of the observed H_2 luminosity and estimated shock velocity:

$$\dot{M}_o \simeq 10^{-6}(1-f_m)\frac{1}{f_c}\left(\frac{L_{H_2}}{10^{-2}\ L_\odot}\right)\left(\frac{v_s}{10\ \mathrm{km\ s^{-1}}}\right)^{-2} M_\odot\ \mathrm{yr}^{-1}. \quad (2)$$

To determine the shock velocity, we use the models of H_2 emission discussed in Section 5.1. In general, the data are best fit by a combination of fast and slow shocks with the slow shock encompassing a larger filling factor within the beam. We have therefore estimated the average shock velocity for each flow by using a filling factor weighted average of the shock velocity based upon the model fits. In Table 4, we provide the observed H_2 luminosity, assumed shock velocity, and derived outflow properties.

In general, we find that the outflows from the Class 0 protostars in the NGC 1333 cloud have values $\dot{M}_w \sim 0.6$–2×10^{-6} $M_\odot$ yr^{-1}. These values are comparable to values estimated in the literature (e.g., Bontemps et al. 1996; Giannini et al. 2001; Hatchell et al. 2007). In some cases measurements include sources within our sample. For example, Giannini et al. (2001) use FIR cooling lines toward IRAS 4 to derive $\dot{M}_w = 0.4$–1.4×10^{-6} $M_\odot$ yr^{-1} where we estimate $\dot{M}_w = 2 \times 10^{-6}$ $M_\odot$ yr^{-1}. The derived mass outflow rates can be related to the mass accretion rate ($\dot{M}_a$) using theoretical models of outflow generation. While the details and results can vary, a typical number is $\dot{M}_o \simeq 0.1$ $\dot{M}_a$ (Pudritz et al. 2007), and our estimates provide $\dot{M}_a \sim 10^{-5}$ $M_\odot$ yr^{-1}. In this regard, di Francesco et al. (2001) independently derived a mass infall rate of 1×10^{-4} $M_\odot$ yr^{-1} toward IRAS 4A using P Cygni spectral line profiles of H_2CO. In addition, Maret et al. (2002) derived an accretion rate of 5×10^{-5} $M_\odot$ yr^{-1} by modeling the FIR water lines emission from IRAS 4A and 4B envelopes. This is in reasonable agreement with our estimate of 2×10^{-5} $M_\odot$ yr^{-1} for this source.

It is useful to place our results in a broader context. Previous estimates of these quantities for molecular outflows have generally used velocity-resolved CO emission to provide a measure of the total H_2 mass in the flow, and used the velocity extent of the lines to trace the kinematics (e.g., Lada 1985; Bontemps et al. 1996). However, there are a number of uncertainties inherent in this method. The CO abundance has been calibrated to H_2 in some clouds (e.g., Frerking et al. 1982), but can vary if some CO remains frozen on grains (e.g., Bergin & Tafalla 2007) or is photodissociated by radiation generated in the shock or leaking through the outflow cavity. In addition, the CO molecules can be excited in both the low temperature natal core and in the warmer outflow. Thus, toward the central core the spectral line contains a mixture of emission from the high-velocity dispersion core and low dispersion core. To some extent these components can

be disentangled, but there is significant uncertainty regarding the outflow mass present at low velocities that also correspond to the core (Lada & Fich 1996). The CO emission itself is often optically thick, even in the extended line wings. Observations of isotopologues are therefore required, but not always available to correct for the effects of optical depth (e.g., Yu et al. 1999; Arce & Goodman 2001). Finally, estimates of the CO velocities are dependent on the outflow inclination. In a handful of cases, this can directly be measured if proper motion data can be used to measure the tangential velocity to compare the observed radial velocity in the spectral lines. In the majority of cases this information is not available, and inclinations have instead been estimated by models of the flow velocity at different inclinations compared with the observed emission distribution (e.g., Cabrit et al. 1988). However, this estimate is also uncertain.

Our measurements do not suffer from any of these uncertainties. The H_2 lines are optically thin and our observations encompass the most emissive H_2 rotational lines, which we simply sum over rotational states and positions to derive the total emission. We have used shock models to calibrate the amount of cooling accounted for by other molecules. In three sources covered by our maps, we have confirmed that the models are accurately reproducing the observed distribution of cooling power. Since H_2 is the dominant species and a primary coolant, we are directly tracing the energy loss in the most abundant species. H_2 does not emit within the core itself and thus we have no line-of-sight contamination. By using the cooling luminosity to trace outflow energetics our measurements are completely independent of the outflow inclination. As an example our momentum flux estimates are a factor of ∼4–8 above values—uncorrected for inclination—derived from CO emission in same flows in NGC 1333 (Hatchell et al. 2007). On the other hand, our estimates are in good agreement the values (corrected for inclination) of Sandell & Knee (2001).

Our conclusion is similar to that of Giannini et al. (2001) who used *ISO* observations of FIR cooling lines as a measure of the total mechanical luminosity. The major difference is that we use spatially resolved observations of H_2 and supplement our results with those of Giannini et al. (2001) to derive the total cooling loss. Given that we have observed the major coolants, the primary uncertainty in the mass loss rate derivation is the assumed shock velocity. The expected range of shock strengths to create the observed H_2 emission is ∼10–50 km s^{-1}, with adopted values of ∼20–30 km s^{-1} (Table 3). We therefore estimate that the mass outflow rate values are accurate to within a factor of 3 (given a distance of 220 pc).

5.3.3. Impact of Flow on Natal Core

It is well known that outflows inject significant energy and momentum in the surrounding cloud (e.g., Lada 1985; Arce et al. 2007; Davis et al. 2008) with some suggestions that these flows drive supersonic motions (Mac Low & Klessen 2004). It is also possible that the outflow is the key player in the disruption of the natal core (e.g., Tafalla & Myers 1997; Fuente et al. 2002). Our data offer a new opportunity to explore the question of the outflow impact on the surrounding material in the specific case of low mass star formation.

The total momentum injected by outflows into a core is given by $P = \dot{P}\,\tau_{\rm dyn} \sim 0.3\ M_\odot$ km s^{-1}, where $\dot{P} = \dot{M}_w\, v_s$ and $\tau_{\rm dyn}$ is the outflow dynamical timescale. Using $\tau_{\rm dyn}$ values from Knee & Sandell (2000), we find P values ranging from 0.1 to 0.4 $M_\odot$ km s^{-1} (see Table 4). If a similar level of outflow activity persists during the lifetime of the embedded phase of $\sim 5 \times 10^5$ yr (Evans et al. 2008) then the total momentum over this phase is ∼4–20 $M_\odot$ km s^{-1}. There is some evidence in the literature of a decline in the outflow momentum flux during the transition from Class 0 to Class I (Bontemps et al. 1996). However, Hatchell & Fuller (2008), with a homogeneous sample of sources in Perseus, do not confirm this result finding similar momentum fluxes for sources with comparable luminosities and masses.

Based on these estimates when the entrained outflowing material slows down to 1 km s^{-1} then it will have swept up 4–20 $M_\odot$ of material. Assuming a typical core mass of ∼5 $M_\odot$ then the outflow is clearly capable of destroying the core during the lifetime of the embedded phase. Of course, the flow will only disperse material in its path and the typical outflow cone angle in these sources is ∼60° (Jørgensen et al. 2007). However, observations suggest that the outflow cone angle increases with age (Velusamy & Langer 1998; Arce & Sargent 2006). Estimates of core masses vary by nearly an order of magnitude in the literature (Lefloch et al. 1998; Sandell & Knee 2001; Walsh et al. 2007) so definitive comparisons within our small sample are difficult. Nonetheless these data clearly suggest that the outflow could be the main mechanism for core dispersal.

To support our assertion that the transfer of outflow momentum to the core is a main mechanism for core dispersal we can also compare the energetics. Tafalla & Myers (1997) demonstrated that the outflow from a massive star (Mon R2) exceeds or is comparable to the gravitational binding energy of its core. Thus, the Mon R2 outflow has likely sculpted that object. However, massive star outflows are more energetic than the low mass objects sampled in our maps and this result may not scale to low mass systems. The average total energy generated by the current generation of outflows in the center of NGC 1333 is $\langle L_{\rm H_2}/f_c \times \tau_{\rm dyn}\rangle = 2 \times 10^{43}$ erg. The gravitational binding energy of a sphere is $\alpha\, GM^2/R$ with $\alpha = 1$ for cores with a r^{-2} density profile (MacLaren et al. 1988), as expected for these embedded protostars. For a typical core mass of ∼5 $M_\odot$ and radius of 0.03 pc the binding energy is $\sim 4 \times 10^{43}$ erg. If we assume that a similar level of activity exists over the lifetime of the embedded phase then the outflow energetics are equal to or even exceed the gravitational energy of the core. In sum, both the flow energetics and momentum suggest that outflows are the primary method for core dispersal. Molecular gas observations show that NGC 1333 cores discussed here are embedded in a much larger but lower density cloud (e.g., Pineda et al. 2008). As typical for GMCs, the cloud binding energy is much greater than those of each individual cores. Thus, the flows which disrupt the cores are not major players in cloud disruption as the cloud momentum and energy far exceed that provided by the current generation of flows over their lifetime.

6. CONCLUSIONS

We have presented *Spitzer*–IRS maps of seven pure rotational H_2 lines in the NGC 1333 star-forming region. These observations cover a region roughly $20' \times 13'$ that encompass a number of YSOs and outflows. We have analyzed these observations using the rotational diagram technique in order to derive the excitation temperature and the H_2 *opr*. Furthermore, these observations have been compared with the predictions of a planar stationary shock model. Finally, we have used the H_2 total luminosity to estimate the mass outflow rates, the mass infall rate

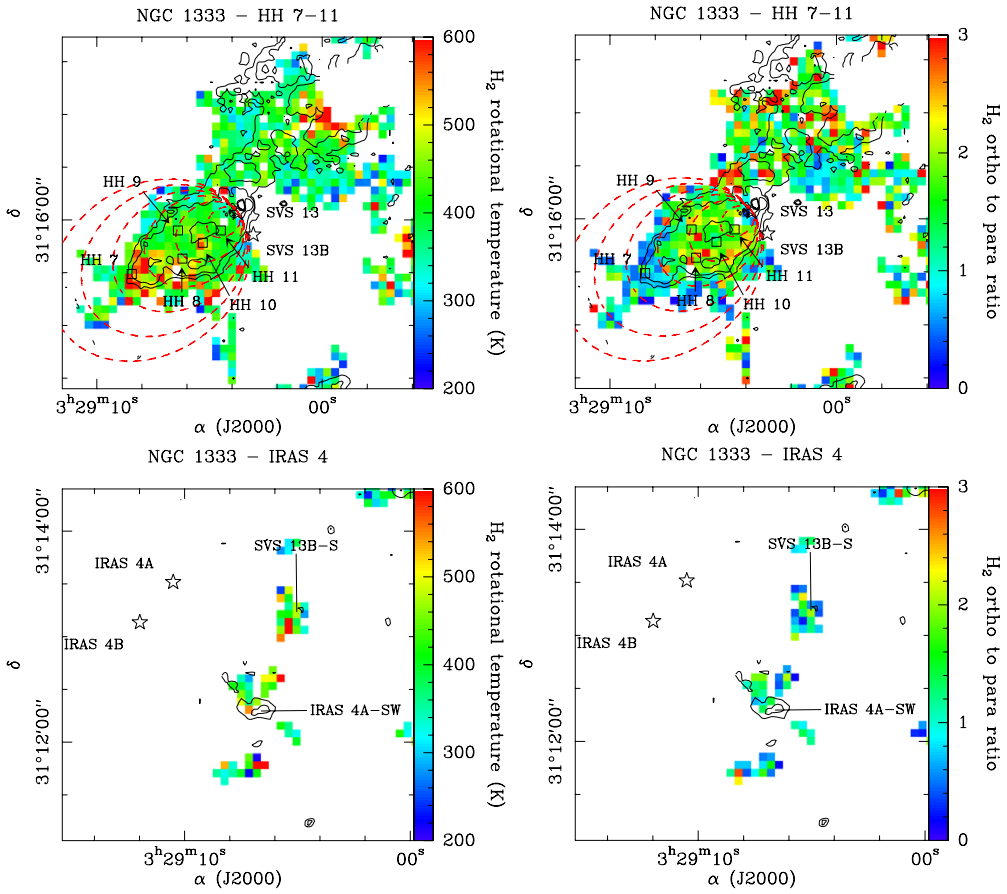

Figure 11. Side-by-side comparison between the rotational temperature and *opr* around SVS 13 (upper panels) and IRAS 4 (lower panels). The position of several HH objects around SVS 13, from Walawender et al. (2005), is indicated. The ellipses that were used to average the *opr* and the rotational temperature (see the Appendix) are shown.

(A color version of this figure is available in the online journal.)

onto the central objects, and the momentum and energy injected into the cores and the cloud. Our main conclusions are as follows.

1. H_2 line emission is detected along several outflows in NGC 1333. In particular, we detect line emission along both lobes of the HH 7-11 outflow, along the south–west lobe of the outflow driven by IRAS 4A, along the north, south, and east lobes of the IRAS 2 outflow, as well as around IRAS 7. In addition, we detect some faint emission south of SVS 13, which is associated with the outflow originating from SVS 13B. Diffuse emission is detected north of this source, and might be associated with this outflow as well.
2. A rotational diagram analysis on several aperture-averaged spectra indicate the presence of at least two gas components toward each position. The warm component has a rotational temperature between ∼300 and 600 K and an *opr* between ∼0.3 and 0.7, while the hot component has a rotational temperature between ∼1000 and 1500 K and an *opr* between ∼1.9 and 2.2.
3. Comparison of the line fluxes measured toward these positions with the predictions of a planar stationary shock model indicate the presence of slow and fast shock components. A good fit of the observation is obtained for an initial *opr* of 0.01 (except in one source where the data are better fit with an initial *opr* of 1), a preshock density of 10^4, and a shock velocity of ∼20 km s^{-1} and ∼45 km s^{-1} the slow and fast shock components, respectively. This indicates, in agreement with earlier studies, that H_2 is mostly in para form in dense molecular clouds (i.e., $opr \lesssim 1$). This is consistent with the predictions of chemical models, provided that the cloud lifetime exceed a few million years.
4. Maps of the rotational temperature and the *opr* in warm components show some important variations of these quantities across the mapped region. We confirm the presence of gas with a relatively high rotational temperature and low *opr* at the tip of the HH 7-11 outflow. This gas is probably "fresh gas" with a low initial *opr* that has been heated up by the passage of a shock, but whose *opr* has not had time to increase significantly. The same feature is observed on both lobes of the IRAS 7 flow, although less clearly. Spatial averages of the *opr* and the rotational temperature along the flow support this hypothesis. Interestingly, no spatial correlation between the two quantities is found.
5. Comparison between the total H_2 luminosity and the luminosity of other lines observed by *ISO* in HH 7-11 and IRAS 4 indicates that between a fourth and half of the total cooling in these outflows occurs through the H_2 lines. Therefore, H_2 lines can be used to estimate the kinetic energy injected into the natal cloud by these flows, as well as outflow mass loss rate which are found to be 0.6–2 × 10^{-6} $M_\odot$ yr^{-1}. The latter quantity also places indirect constraints on the mass accretion rate onto the

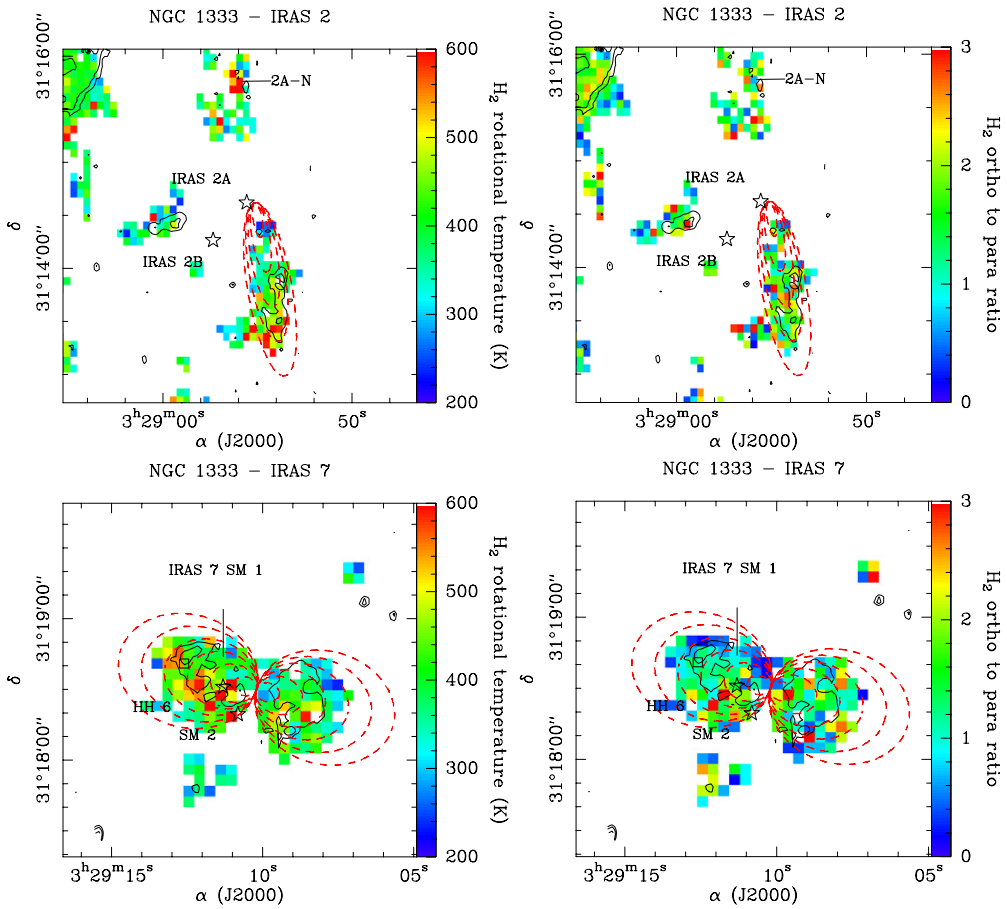

Figure 12. Same as Figure 11 for the IRAS 2 (upper panels) and IRAS 6 (lower panels).
(A color version of this figure is available in the online journal.)

protostar: dynamical models predict that the outflow mass loss rate is typically 10 times lower than the accretion rate. Using the dynamical timescale obtained from millimeter observations, we derived the total momentum injected in the clouds by the outflows, and compared it to the core and cloud binding energy. We found that outflows have the potential to disrupt individual cores, but are probably not major players in cloud disruption.

This work is based on observations made with the *Spitzer Space Telescope*, which is operated by the Jet Propulsion Laboratory, California Institute of Technology under a contract with NASA. Support for this work was provided by NASA through an award issued by JPL/Caltech for program #20378.

Facilities: Spitzer (IRS)

APPENDIX

VARIATION OF THE *opr* WITH TEMPERATURE

As mentioned in Section 4.2, some important spatial variations in both the *opr* and the rotational temperature are observed in NGC 1333. In particular, we observe, at a tip of the HH 7-11 outflow, a bow shocklike region with a low *opr* (∼0.5) and high rotational temperature (∼650 K; see Figure 11). This low *opr* region wraps nicely around the H_2 $S(1)$ rotational line emission, and suggests that it corresponds to gas which has been recently heated up by the passage of a shock, but whose *opr* has not had time to reach the equilibrium value. Interestingly, this region also corresponds to the part of the flow where the rotational temperature is the highest. Around IRAS 7, we also observe low *opr* regions around the H_2 $S(1)$ emission contours (see Figure 12), but variations from 1 pixel to the other are important and it is less clear if this region correspond to high temperature gas, like in HH 7-11.

It is interesting to compare the variations of the *opr* and the rotational temperature as a function of the position of the flow in a more quantitative fashion. In order to do this, we have computed the average of the *opr* and rotational temperature along the outflows that show some degree of symmetry, and where both quantities were measured in a sufficient number of pixels. In order to "capture" the spatial variations, we have defined a series of ellipses of the same eccentricity, oriented along the flow and with an apex that is centered on the outflow driving source. The eccentricity of the ellipses has been chosen in order to match the shape of each outflow lobe as observed in the H_2 $S(1)$ emission. We have then computed the average of the *opr* ratio and the rotational temperature in the region between two consecutive ellipses (that is two ellipses with different major axes). In Figure 11 and 12, we show how those ellipses where defined for HH 7-11, IRAS 7 (east and west lobes), and IRAS 2 (south lobe). We have not computed the average for the other outflow lobes, because the *opr* ratio and the rotational temperature had greater uncertainties.

Figure 13 shows the average *opr* and rotational temperature, as a function of the ellipse semimajor axis. Along the HH 7-11 outflow, we see a sharp drop in the average *opr* ratio 35″ from SVS 13. Interestingly, the temperature does not seem

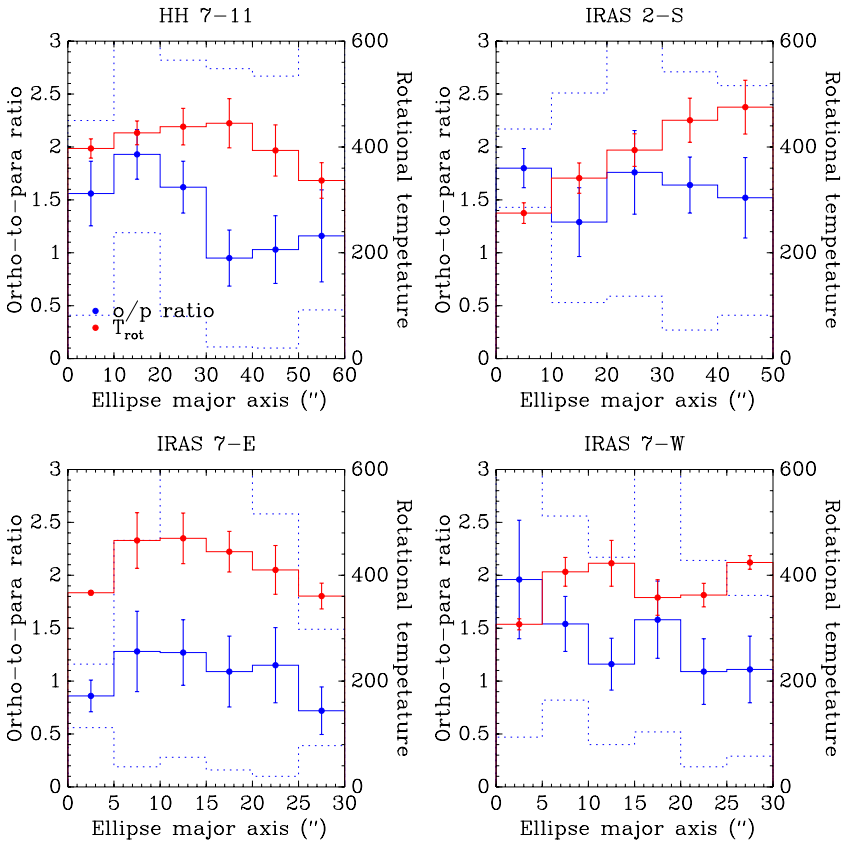

Figure 13. Average H_2 *opr* (blue histograms in the solid lines) and rotational temperature (red histograms) between consecutive ellipses of the same eccentricity, as a function of the ellipse semimajor axis. The error bars are 1σ standard deviations computed from the variance in each bin (i.e., the region between two ellipses). The blue histogram in the dotted lines shows the maximum and minimum values of the *opr* in each bin.

(A color version of this figure is available in the online journal.)

to be correlated with the *opr*. It increases slightly 0″ and 35″ (although at a 1σ level), and then starts to decrease. The highest temperature is reached where the *opr* ratio is minimal. Presumably, the hottest point corresponds to the shock front. In the postshock gas, the para-to-ortho conversion has increased the *opr*, but the conversion is incomplete and the ratio does not reach the LTE value. In the preshock gas the *opr* has also probably increased with respect to its initial value, but has not had time to reach the same value that we see in the postshock gas (i.e., ∼2). Note that for a preshock density of 10^4 cm^{-3}, and a shock velocity of 20 km s^{-1}, the model predicts a shock front width—defined as the region of the shock where the temperature is greater than 1000—of $\sim 10^3$ AU, i.e., about 5″ at the distance of NGC 1333.

The interpretation of the *opr* and rotational temperature along the other flows is less straightforward. We see an increase of the rotational temperature along the IRAS 4 lobe, but the maximum temperature is reached at the tip of the outflow; farther away no H_2 emission is detected and the rotational temperature and the *opr* could not be determined. Unlike the HH 7-11, the average *opr* ratio is roughly constant, and is ∼2. The temperature in the east lobe of IRAS 7 flow seems to slightly decrease (note that the first ellipse contains only a couple of points, so the average is not very meaningful in this bin), while the *opr* is almost constant. On the other hand, the *opr* ratio and temperature may vary in a similar fashion that in HH 7-11. The *opr* drops sharply between 5″and 15″, while the temperature seems to slightly increase in the same region. However, further away the temperature appears to be roughly constant.

REFERENCES

Arce, H. G., & Goodman, A. A. 2001, ApJ, 554, 132
Arce, H. G., & Sargent, A. I. 2006, ApJ, 646, 1070
Arce, H. G., Shepherd, D., Gueth, F., Lee, C.-F., Bachiller, R., Rosen, A., & Beuther, H. 2007, in Protostars and Planets V, ed. B. Reipurth, D. Jewitt, & K. Keil (Tucson, AZ: Univ. Arizona Press), 245
Aspin, C., Sandell, G., & Russell, A. P. G. 1994, A&AS, 106, 165
Bachiller, R., Codella, C., Colomer, F., Liechti, S., & Walmsley, C. M. 1998a, A&A, 335, 266
Bachiller, R., Gueth, F., Guilloteau, S., Tafalla, M., & Dutrey, A. 2000, A&A, 362, L33
Bachiller, R., Guilloteau, S., Gueth, F., Tafalla, M., Dutrey, A., Codella, C., & Castets, A. 1998b, A&A, 339, L49
Bergin, E. A., & Tafalla, M. 2007, ARA&A, 45, 339
Blake, G. A., Sandell, G., van Dishoeck, E. F., Groesbeck, T. D., Mundy, L. G., & Aspin, C. 1995, ApJ, 441, 689
Bontemps, S., Andre, P., Terebey, S., & Cabrit, S. 1996, A&A, 311, 858
Cabrit, S., Goldsmith, P. F., & Snell, R. L. 1988, ApJ, 334, 196
Cernis, K. 1990, Ap&SS, 166, 315
Davis, C. J., Scholz, P., Lucas, P., Smith, M. D., & Adamson, A. 2008, MNRAS, 387, 954
di Francesco, J., Myers, P. C., Wilner, D. J., Ohashi, N., & Mardones, D. 2001, ApJ, 562, 770
Draine, B. T., & McKee, C. F. 1993, ARA&A, 31, 373
Evans, N. J. II, et al. 2009, ApJS, 18, 321
Flower, D. R., & Pineau des Forêts, G. 2003, MNRAS, 343, 390
Flower, D. R., Pineau Des Forêts, G., & Walmsley, C. M. 2006, A&A, 449, 621
Frerking, M. A., Langer, W. D., & Wilson, R. W. 1982, ApJ, 262, 590
Fuente, A., Martın-Pintado, J., Bachiller, R., Rodrıguez-Franco, A., & Palla, F. 2002, A&A, 387, 977
Giannini, T., Nisini, B., & Lorenzetti, D. 2001, ApJ, 555, 40
Gredel, R. 1996, A&A, 305, 582
Gutermuth, R. A., et al. 2008, ApJ, 674, 336

Hartmann, L., Ballesteros-Paredes, J., & Bergin, E. A. 2001, ApJ, 562, 852
Hatchell, J., & Fuller, G. A. 2008, A&A, 482, 855
Hatchell, J., Fuller, G. A., & Richer, J. S. 2007, A&A, 472, 187
Henkel, C., Guesten, R., & Haschick, A. D. 1986, A&A, 165, 197
Higdon, S. J. U., et al. 2004, PASP, 116, 975
Hodapp, K.-W., & Ladd, E. F. 1995, ApJ, 453, 715
Houck, J. R., et al. 2004, ApJS, 154, 18
Jennings, R. E., Cameron, D. H. M., Cudlip, W., & Hirst, C. J. 1987, MNRAS, 226, 461
Jørgensen, J. K., Hogerheijde, M. R., Blake, G. A., van Dishoeck, E. F., Mundy, L. G., & Schöier, F. L. 2004, A&A, 415, 1021
Jørgensen, J. K., et al. 2007, ApJ, 659, 479
Kaufman, M. J., & Neufeld, D. A. 1996, ApJ, 456, 611
Khanzadyan, T., Smith, M. D., Davis, C. J., Gredel, R., Stanke, T., & Chrysostomou, A. 2003, MNRAS, 338, 57
Knee, L. B. G., & Sandell, G. 2000, A&A, 361, 671
Kristensen, L. E., Ravkilde, T. L., Field, D., Lemaire, J. L., & Pineau Des Forêts, G. 2007, A&A, 469, 561
Lada, C. J. 1985, ARA&A, 23, 267
Lada, C. J., & Fich, M. 1996, ApJ, 459, 638
Langer, W. D., Castets, A., & Lefloch, B. 1996, ApJ, 471, L111
Le Bourlot, J., Pineau des Forêts, G., & Flower, D. R. 1999, MNRAS, 305, 802
Lefloch, B., Castets, A., Cernicharo, J., Langer, W. D., & Zylka, R. 1998, A&A, 334, 269
Lefloch, B., Cernicharo, J., Cabrit, S., Noriega-Crespo, A., Moro-Martín, A., & Cesarsky, D. 2003, ApJ, 590, L41
Liseau, R., Sandell, G., & Knee, L. B. G. 1988, A&A, 192, 153
MacLaren, I., Richardson, K. M., & Wolfendale, A. W. 1988, ApJ, 333, 821
Mac Low, M.-M., & Klessen, R. S. 2004, Rev. Mod. Phys., 76, 125
Maret, S., & Bergin, E. A. 2007, ApJ, 664, 956
Maret, S., Ceccarelli, C., Caux, E., Tielens, A. G. G. M., & Castets, A. 2002, A&A, 395, 573
Molinari, S., et al. 2000, ApJ, 538, 698
Neufeld, D. A., Hollenbach, D. J., Kaufman, M. J., Snell, R. L., Melnick, G. J., Bergin, E. A., & Sonnentrucker, P. 2007, ApJ, 664, 890
Neufeld, D. A., Melnick, G. J., & Harwit, M. 1998, ApJ, 506, L75
Neufeld, D. A., et al. 2006, ApJ, 649, 816
Pineda, J. E., Caselli, P., & Goodman, A. A. 2008, ApJ, 679, 481
Pudritz, R. E., Ouyed, R., Fendt, C., & Brandenburg, A. 2007, in Protostars and Planets V, ed. B. Reipurth, D. Jewitt, & K. Keil (Tucson, AZ: Univ. Arizona Press), 277
Rodríguez, L. F., Anglada, G., & Curiel, S. 1999, ApJS, 125, 427
Sandell, G., & Knee, L. B. G. 2001, ApJ, 546, L49
Sandell, G., Knee, L. B. G., Aspin, C., Robson, I. E., & Russell, A. P. G. 1994, A&A, 285, L1
Schofield, K. 1967, Planet. Space Sci., 15, 643
Smith, M. D., Brand, P. W. J. L., & Moorhouse, A. 1991, MNRAS, 248, 451
Smith, M. D., Khanzadyan, T., & Davis, C. J. 2003, MNRAS, 339, 524
Strom, S. E., Vrba, F. J., & Strom, K. M. 1976, AJ, 314
Tafalla, M., & Myers, P. C. 1997, ApJ, 491, 653
Timmermann, R. 1998, ApJ, 498, 246
Velusamy, T., & Langer, W. D. 1998, Nature, 392, 685
Walawender, J., Bally, J., & Reipurth, B. 2005, AJ, 129, 2308
Walsh, A. J., Myers, P. C., Di Francesco, J., Mohanty, S., Bourke, T. L., Gutermuth, R., & Wilner, D. 2007, ApJ, 655, 958
Weingartner, J. C., & Draine, B. T. 2001, ApJ, 548, 296
Werner, M. W., et al. 2004, ApJS, 154, 1
Wilgenbus, D., Cabrit, S., Pineau des Forêts, G., & Flower, D. R. 2000, A&A, 356, 1010
Yu, K. C., Billawala, Y., & Bally, J. 1999, AJ, 118, 2940